



Universiteit
Leiden
The Netherlands

Early-forming massive stars suppress star formation and hierarchical cluster assembly

Lewis, S.C.; McMillan, S.L.W.; Mac Low, M.-M.; Cournoyer-Cloutier, C.; Polak, B.; Wilhelm, M.J.C.; ... ; Wall, J.E.

Citation

Lewis, S. C., McMillan, S. L. W., Mac Low, M. -M., Cournoyer-Cloutier, C., Polak, B., Wilhelm, M. J. C., ... Wall, J. E. (2023). Early-forming massive stars suppress star formation and hierarchical cluster assembly. *The Astrophysical Journal*, 944(2).
doi:10.3847/1538-4357/acb0c5

Version: Publisher's Version
License: [Creative Commons CC BY 4.0 license](https://creativecommons.org/licenses/by/4.0/)
Downloaded from: <https://hdl.handle.net/1887/3715331>

Note: To cite this publication please use the final published version (if applicable).



Early-forming Massive Stars Suppress Star Formation and Hierarchical Cluster Assembly

Sean C. Lewis¹ , Stephen L. W. McMillan¹ , Mordecai-Mark Mac Low^{1,2,3} , Claude Courmoyer-Cloutier⁴ , Brooke Polak^{2,5} , Martijn J. C. Wilhelm⁶ , Aaron Tran³ , Alison Sills⁴ , Simon Portegies Zwart⁶ , Ralf S. Klessen^{5,7} , and Joshua E. Wall¹

¹ Department of Physics, Drexel University, Philadelphia, PA, USA; sean.phys@gmail.com

² Department of Astrophysics, American Museum of Natural History, New York, NY, USA

³ Department of Astronomy, Columbia University, New York, NY, USA

⁴ Department of Physics & Astronomy, McMaster University, Hamilton, ON, Canada

⁵ Universität Heidelberg, Zentrum für Astronomie, Institut für Theoretische Astrophysik, Albert-Ueberle-Straße 2, D-69120 Heidelberg, Germany

⁶ Leiden Observatory, Leiden University, P.O. Box 9513, 2300 RA Leiden, The Netherlands

⁷ Universität Heidelberg, Interdisziplinäres Zentrum für Wissenschaftliches Rechnen, Im Neuenheimer Feld 205, D-69120 Heidelberg, Germany

Received 2022 November 4; revised 2022 December 23; accepted 2023 January 4; published 2023 February 27

Abstract

Feedback from massive stars plays an important role in the formation of star clusters. Whether a very massive star is born early or late in the cluster formation timeline has profound implications for the star cluster formation and assembly processes. We carry out a controlled experiment to characterize the effects of early-forming massive stars on star cluster formation. We use the star formation software suite `Torch`, combining self-gravitating magnetohydrodynamics, ray-tracing radiative transfer, N -body dynamics, and stellar feedback, to model four initially identical $10^4 M_{\odot}$ giant molecular clouds with a Gaussian density profile peaking at 521.5 cm^{-3} . Using the `Torch` software suite through the `AMUSE` framework, we modify three of the models, to ensure that the first star that forms is very massive (50, 70, and $100 M_{\odot}$). Early-forming massive stars disrupt the natal gas structure, resulting in fast evacuation of the gas from the star-forming region. The star formation rate is suppressed, reducing the total mass of the stars formed. Our fiducial control model, without an early massive star, has a larger star formation rate and total efficiency by up to a factor of 3, and a higher average star formation efficiency per freefall time by up to a factor of 7. Early-forming massive stars promote the buildup of spatially separate and gravitationally unbound subclusters, while the control model forms a single massive cluster.

Unified Astronomy Thesaurus concepts: [Astronomical simulations \(1857\)](#); [Young massive clusters \(2049\)](#); [Star forming regions \(1565\)](#); [Massive stars \(732\)](#)

1. Introduction

The process of star cluster formation involves a wide range of physical processes that are not entirely understood. Reviews of the field include those by Mac Low & Klessen (2004), McKee & Ostriker (2007), Portegies Zwart et al. (2010), Klessen et al. (2016), Krumholz et al. (2019), Girichidis et al. (2020), and Krause et al. (2020).

A star cluster requires millions of years to form, and it is deeply embedded in dense gas and dust for a significant portion of that time (Lada & Lada 2003; Chevance et al. 2020). Therefore, it is difficult to understand the formation process by relying on observations. Computational models can provide essential insights to this process. These models have established that cloud properties and galactic influences strongly regulate the conversion of gas into stars within clouds that are undergoing hierarchical collapse. These include the turbulent velocity field (Ostriker et al. 1999; Klessen et al. 2000), the magnetic field strength and orientation (McKee 1999), the gas density profile (Chen et al. 2021), the multiphase nature of the interstellar medium (Ostriker et al. 2010), galactic mergers (Dobbs et al. 2020), the galactic gravity field (Li & Gnedin 2019), and galactic jets (Mandal et al. 2021).

The feedback from massive stars probably dominates the self-regulation of the star formation process. Computational models have shown that massive stellar feedback, including ionizing radiation (Matzner 2002; Dale et al. 2012), nonionizing radiation (Howard et al. 2018), stellar winds (Dale et al. 2014; Rahner et al. 2017), and supernovae (Rogers & Pittard 2013; Smith et al. 2018), can disrupt the parental giant molecular clouds (GMCs) and shut down star formation. For a general review of the feedback models that are employed in many current star cluster formation simulations, see Dale (2015). Without these mechanisms, the gravitational collapse of the cloud would continue unimpeded, converting all the natal gas into stars, in stark contrast to the observations of such regions (Ostriker et al. 2010; Chevance et al. 2022).

Massive stellar feedback is also thought to regulate the subcluster structure and assembly. The hierarchical assembly of clusters has been observed (Bressert et al. 2010; Longmore et al. 2014; Gouliermis et al. 2017) and demonstrated computationally (Maschberger et al. 2010; Vázquez-Semadeni et al. 2017; Grudić et al. 2018; Howard et al. 2018; Vázquez-Semadeni et al. 2019; Chen et al. 2021; Dobbs et al. 2022; Guszejnov et al. 2022). Gas evacuation (via stellar feedback) is crucial to the completion of the assembly process (Grudić et al. 2018; Krause et al. 2020). In addition, it has been established that how the gas is removed from a cluster can potentially affect the cluster structure (Smith et al. 2013). Rapidly evacuated gas can result in cluster destruction or dissolution,



Original content from this work may be used under the terms of the [Creative Commons Attribution 4.0 licence](#). Any further distribution of this work must maintain attribution to the author(s) and the title of the work, journal citation and DOI.

through the unbinding of stars (Lada & Lada 2003; Portegies Zwart et al. 2010; Banerjee & Kroupa 2017). Gavagnin et al. (2017) have also found a weak correlation between the feedback strength and the unbinding of stars, while Li et al. (2019) saw some dispersal of stars at the highest feedback levels in their parameter study. However, there has been little research into the effects resulting from when the gas removal occurs. With our computational model, we test the effects of early-forming massive stars on cluster formation and the hierarchical cluster assembly process.

Massive star feedback mechanisms have been shown to slow star formation and contribute to the destruction of the natal cloud. In order to accurately model the star cluster formation, each feedback mechanism must be modeled simultaneously, within the same computational model. Doing so at the appropriate level of sophistication provides a more realistic star cluster formation framework, from which simulations can be constructed. Several recent efforts have created such a framework, by combining multiple massive star feedback mechanisms with magnetohydrodynamical (MHD) solvers (Rogers & Pittard 2013; Dale et al. 2014; Grudić et al. 2021; Lancaster et al. 2021). Using the AMUSE framework (Portegies Zwart et al. 2009; Pelupessy et al. 2013; Portegies Zwart et al. 2013; Portegies Zwart & McMillan 2018), we have constructed a hybrid N -body and MHD simulation environment for modeling cluster formation, called `Torch` (Wall et al. 2019, 2020). We combine stellar evolution, massive stellar radiative feedback, winds, and supernovae into an adaptive-mesh MHD framework, and couple this with high-precision N -body dynamics, allowing us to follow the dynamics of individual stars within an actively forming cluster that exposes the gas to feedback from the massive stars. We test the hypothesis that the timing of the massive star formation plays a vital role in the star formation and star cluster assembly processes, because, once formed, massive stars disrupt the natal gas cloud, limit the global star formation efficiency (SFE), and promote the formation of stellar subclusters, while hindering their assembly into a young massive cluster.

We test the impacts of early-forming massive stars by comparing simulations with identical initial conditions but varying masses for the first formed star, either by randomly choosing the mass from the initial mass function (IMF) in our fiducial run or by forcing the star to have a mass of 50, 70, or 100 M_{\odot} .

We describe our initial simulation conditions and parameter space in Section 2. We analyze the effects of early-forming massive stars on gas and star cluster formation in Section 3. We discuss our results, compare them to previous works, and note the limitations of our model in Section 4. Finally, we conclude in Section 5.

2. Methods

`Torch`⁸ (Wall et al. 2019) couples the adaptive-mesh MHD code FLASH (Fryxell et al. 2000), including modules that implement heating and cooling, ray-traced radiative transfer (Baczynski et al. 2015), and sink particle creation (Federrath et al. 2010) within the AMUSE framework. Within AMUSE, we also use the N -body dynamics solver `ph4` (McMillan et al. 2012), the

binary and close encounter modules `multiple` (Portegies Zwart & McMillan 2018) and `smalln` (Hut et al. 1995; McMillan & Hut 1996), as well as the stellar evolution module `SeBa` (Portegies Zwart & Verbunt 1996).

FLASH is integrated into AMUSE using the hierarchical coupling strategy (Portegies Zwart et al. 2020), which is a generalization of the gravity bridge scheme developed by Fujii et al. (2007). With this coupling, we are able to model magnetized, self-gravitating, and radiatively heated and cooled GMCs, while also forming stars from the gas and resolving individual stellar dynamics. Within FLASH, we use an HLLD Reimann solver (Miyoshi & Kusano 2005), with order 3 PPM reconstruction (Colella & Woodward 1984). If a particularly strong shock occurs, which triggers numerical instability, we briefly switch to the more diffusive HLL solver (Einfeldt et al. 1991), with first-order Godunov reconstruction (Godunov & Bohachevsky 1959). Our method of converting the collapsing gas into stars uses FLASH’s sink particle module (Federrath et al. 2010), which replaces the Jeans-unstable gas (Truelove et al. 1997) with a sink particle (hereafter, “sink”) with a mass equivalent to the replaced gas (see Federrath et al. 2010 for details of the sink creation and accretion criteria).

The adaptive mesh is required to refine such that the Truelove et al. (1997) length is resolved by four or more cells. The computational domain is a cube of size 17.5 pc. At the top refinement level, the entire grid is represented by a single block of 16^3 cells. Each successive refinement level can break a block into four smaller blocks. Our runs have a maximum refinement level of three, for which the cells are 0.27 pc on a side. The outer edges of the computational domain are governed by outflow boundary conditions, to allow gas to properly escape from the star-forming region.

We evolve four simulations with identical initial conditions. In the first, we treat the simulation as a standard `Torch` run, with the usual physical prescriptions. In the other runs, the first star to be born has a mass of 50, 70, or 100 M_{\odot} (referred to as the 50 M , 70 M , and 100 M runs, respectively). We evolve the simulations until star formation ceases or the forced massive star goes supernova (~ 6 Myr total, or 4 Myr after star formation begins). In the case of the 100 M run, nearly all the gas and stars eventually escape the computational domain. This allows for large time steps and a simulation that extends farther in time than the other runs.

2.1. Initial Conditions

We initialize a $10^4 M_{\odot}$ GMC as a spherical cloud with a radius of 7.25 pc and a Gaussian density distribution (Bate et al. 1995) with a standard deviation of 4.89 pc. The cloud is also surrounded by a low-density background medium. All the gas has solar metallicity, which remains constant throughout the simulations. No background galactic gravitational potential is applied. We initialize the cloud and background medium to be in pressure and thermal equilibrium, and we choose the gas densities and temperature accordingly. The spherical cloud is in the cold neutral medium phase, with the central gas density being 521.5 cm^{-3} at a temperature of 20.6 K. The cloud edge density is one-third the central density. The low-density, higher-temperature surrounding gas is in the warm neutral medium phase, with a density of 1.3 cm^{-3} and a temperature of 6105.3 K. We apply a turbulent Kolmogorov velocity distribution (R. Wunsch 2015, personal communication) to the dense gas, such that it is subvirial, with a virial ratio

⁸ <https://bitbucket.org/torch-sf/torch/src/main>, using commit 811d35ea069ca4a7e099e62bb4f0580f0a49cf29 for the runs presented in this paper.

$\alpha = 2T/|U| = 0.12$, where T is the total kinetic energy and $|U|$ is the magnitude of the potential energy. Low-virial parameter clouds are appropriate for regions containing massive star formation (Kauffmann et al. 2013), and such low-virial parameter clouds have been cataloged (Roman-Duval et al. 2010; Wienen et al. 2012). A subvirial initial state provides an environment in which star formation readily occurs in dense regions, and it tends to reduce the effects of early-forming massive stars, due to the reduced penetrating power of the feedback mechanisms through the dense gas. We initialize the cloud with a uniform $3 \mu\text{G}$ magnetic field along the z -axis, and we allow the gas turbulence to mix the field, mirroring the setup defined by Wall et al. (2019) and Wall et al. (2020).⁹ We also apply a background far-UV radiation field with a constant flux of $1.7G_0$ (Draine 1978), where $G_0 = 1.6 \times 10^{-3} \text{ erg s}^{-1}$ is the Habing (1968) flux. We estimate the extinction of the far-UV flux using the local Jeans length (Truelove et al. 1997). We also assume a constant gas ionization rate due to cosmic rays $\zeta = 10^{-17} \text{ s}^{-1}$.

2.2. Sink Properties and Star Formation

As the dense gas collapses, sinks may form at the highest levels of refinement if the conditions detailed in Section 2.2 of Federrath et al. (2010) are satisfied. The sinks in our simulation have accretion radii of 0.67 pc. They are fixed to grid cell centers and move at each time step to the cell of the lowest gravitational potential within their accretion radii. Sinks also merge together if their radii overlap.

Once a sink forms, we assign to it a list of random stellar masses, sampled from the Kroupa (2002) IMF, with a maximum of $150 M_\odot$ and a minimum of $0.08 M_\odot$, following Weidner & Kroupa (2006), Sormani et al. (2017), and Wall et al. (2019). Once a sink has accreted enough material to match or exceed the mass of the next star to be formed, a nonaccreting star particle (hereafter, “star”) is placed on the grid inside the sink radius, and the same mass is removed from the sink. The initial position of a new star is randomly sampled from a spherical Gaussian distribution positioned at the center of the sink. The initial velocity components of a star are sampled from a Gaussian distribution, with a scale set to the speed of sound of the gas on which its parent sink is sitting. The sink can then continue to accrete gas, and the star is permitted to move throughout the computational domain under the gravitational influences of the gas, sinks, and other stars. Sink accretion may continue until the local gas reservoir is exhausted or the gas is heated by ionization or shocks from a massive star.

Stars are not tied to the structure of the computational mesh, but they do exert gravitational forces on and experience gravitational forces from the gas as well as other stars and sinks. Stars start at zero-age main sequence (ZAMS). Stars above $7 M_\odot$ produce feedback effects, in the forms of photoelectric heating and ionizing fluxes, stellar winds, and supernovae. These feedback mechanisms are injected into the computational domain, based on the star’s evolution, as modeled in SeBa.¹⁰ Since the stars are placed at ZAMS,

massive stars begin their feedback the instant that they are placed onto the grid. We therefore do not resolve any earlier feedback effects that take place during the massive star accretion phase. SeBa also models the deaths of massive stars, taking stellar mass, end-of-life composition, and metallicity into account when determining supernova types. Only the early-forming massive stars reach the supernova stage in our runs. They all detonate as supernovae, as their metallicity places them outside the regime of massive stars that directly collapse to a black hole (Heger et al. 2003).

2.3. Early-forming Massive Stars

Spawning a massive star in a typical Torch run is a rare event. Each sink has tens of thousands of stars on its stellar mass list, but only a few dozen are very massive ($\geq 50 M_\odot$) and they are randomly placed within the list. Therefore, within our computational model, it is unlikely—but possible—for a sink to have a very massive star as one of the first entries on its mass list. To explore the effects of the early formation of a very massive star, we force the first formed sink to have either a 50, 70, or $100 M_\odot$ star as the first entry on its mass list. Before the sink begins accreting gas for the 50, 70, or $100 M_\odot$ star, our implementation allows for the formation of six stars (the most massive of which is $0.8 M_\odot$, with an average mass of $0.45 M_\odot$).

The chosen parent sink for the very early-forming massive star is also the first sink to form. This is a deliberate choice, as this sink forms near the center of the collapsing cloud, thus it has a substantial supply of infalling material to accrete, and so it can spawn the very massive star as the first to be born from the sink. Other sinks are still able to form elsewhere in the collapsing cloud, if the formation conditions are satisfied. Indeed, another sink does form around 6 to 7 pc from and 500 kyr after the parent. In each forced run, this sink is able to form $\sim 24 M_\odot$ of stars (29 stars in total, with the most massive being $9.8 M_\odot$), before the early-forming massive star forms.

3. Analysis

Visual inspections of the simulations at a characteristic time reveal the increased destructive effects of early-forming massive stars on both the gas and the hierarchical assembly of the resulting star clusters. Figure 1 shows the column densities of each run at the simulation time $t = 4.51 \text{ Myr} = 2\tau_{\text{ff}}$, where τ_{ff} is the freefall time of the initial gas cloud. At this characteristic time, the gas is more fragmented in the runs containing early-forming massive stars ($50 M$, $70 M$, and $100 M$), with the $100 M$ run showing the most fragmentation. We further choose $2\tau_{\text{ff}}$ as the snapshot for analysis, since subclusters begin exiting the computational domain after this time.

In the fiducial run, the gas remains present in the central regions of the cloud, even at the end of the run. The stars formed in the fiducial run collect into a single large cluster, while the forced runs result in several localized associations of stars.

In the forced runs, since the sink selected to form the early massive star is close to the center of mass of the cloud, the early-forming massive star also forms near the center of mass. Though the parent sink does pick up a drift velocity of a few kilometers per second as it falls into the cloud, once the early

⁹ Runs M3f and M3f2 in Wall et al. (2020) did not include magnetic fields, due to an incorrect initialization procedure; this oversight has been corrected, so all our runs begin with the uniform magnetic field.

¹⁰ We have updated the time-step determination process in Torch to ensure that massive stars take small enough SeBa evolution steps compared to the current gas dynamical time step to resolve evolutionary changes in their properties.

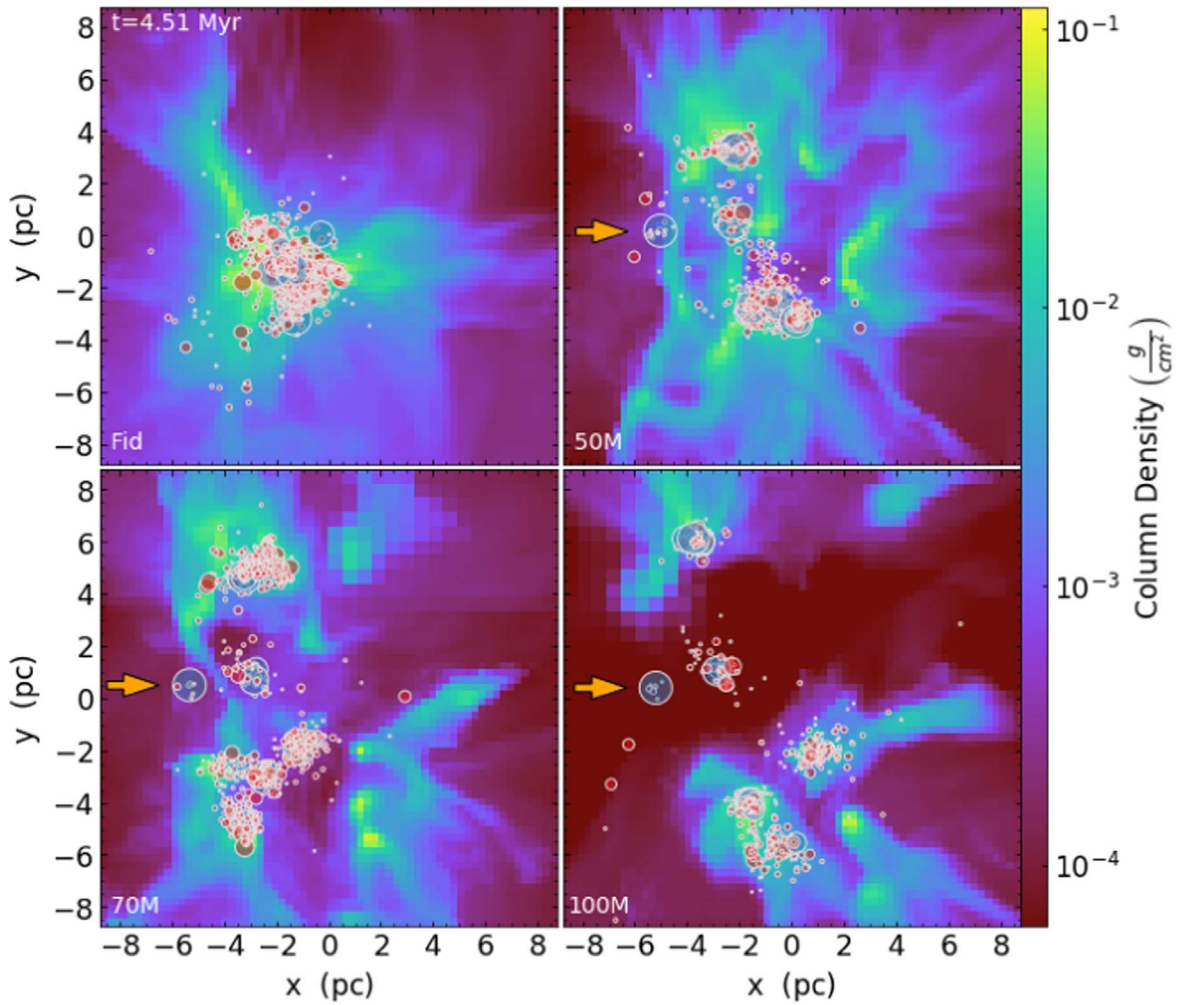


Figure 1. Snapshot of the fiducial run and the early-forming massive star runs for $50 M$, $70 M$, and $100 M$ at $2\tau_{\text{ff}}$. All the runs start from identical initial conditions. The gas column density as well as the stars are plotted. The stars denoted by red circles have masses $< 7 M_{\odot}$ and do not produce any form of feedback in our model. The stars denoted by blue circles have masses $> 7 M_{\odot}$ and produce ionizing radiation, winds, and supernovae. The plotted star sizes are scaled by the star’s mass. The orange arrows highlight the forced massive star in each of the forced runs.

massive star forms, it rapidly evacuates the cloud center of gas, thereby removing the gas potential as well. As a result, the massive star and its parent sink (in all three of the forced runs) continue to drift as the simulation progresses. The early-forming massive stars at $2\tau_{\text{ff}}$ (about 2.5 Myr after their formation) can be seen in Figures 1 and 2, indicated by orange arrows. In the time since their formation, they are all able to drift several parsecs from their initial positions (within 1 pc of the simulation origin). The stars that are born after the early-forming massive star still collect in clumped groups, but more readily form in gas clumps that build up on the outskirts of the original spherical cloud, rather than at the density center, as in the fiducial run.

Figure 2 shows the density of the fully ionized gas as a slice through the computational domain at $z = 0$ pc. At $2\tau_{\text{ff}}$, the early-forming massive stars have ionized a significant portion of the computational domain and their low-density ionized wind bubble is dominant, particularly in the $70 M$ and $100 M$ runs. Each forced run still has regions of partially or fully shielded gas that have not been fully ionized, with the $50 M$ run having the most extensive regions of gas that are not fully ionized. In the fiducial run, a distinct wind bubble is not yet visible, as the massive stars in the central cluster have not had

time to carve away the surrounding dense gas. However, their ionizing radiation has been able to penetrate and fully ionize the dense gas below the cluster, while large portions of the $+y$ quadrants are still partially ionized or shielded neutral gas.

So while the fiducial run has not yet begun to mechanically disrupt the gas surrounding the main cluster, ionizing feedback has still penetrated into portions of the grid. Meanwhile, the $50 M$, $70 M$, and $100 M$ runs show extensive ionization throughout the region and clear mechanical disruption via their developing wind bubbles, with the level of disruption seeming to increase monotonically with the increasing forced star mass.

To quantify the effects of the early-forming massive stars, we analyze the energetics and behavior of the gas as well as the conversion of the gas into stars. We also quantify the effects of early-forming massive stars on the hierarchical assembly of subclusters, by identifying clusters and investigating their properties.

3.1. Gas Disruption and Expulsion

We measure the total energy of all the gas in the computational domain by summing its mechanical energy, thermal energy, magnetic energy, and the gravitational energy

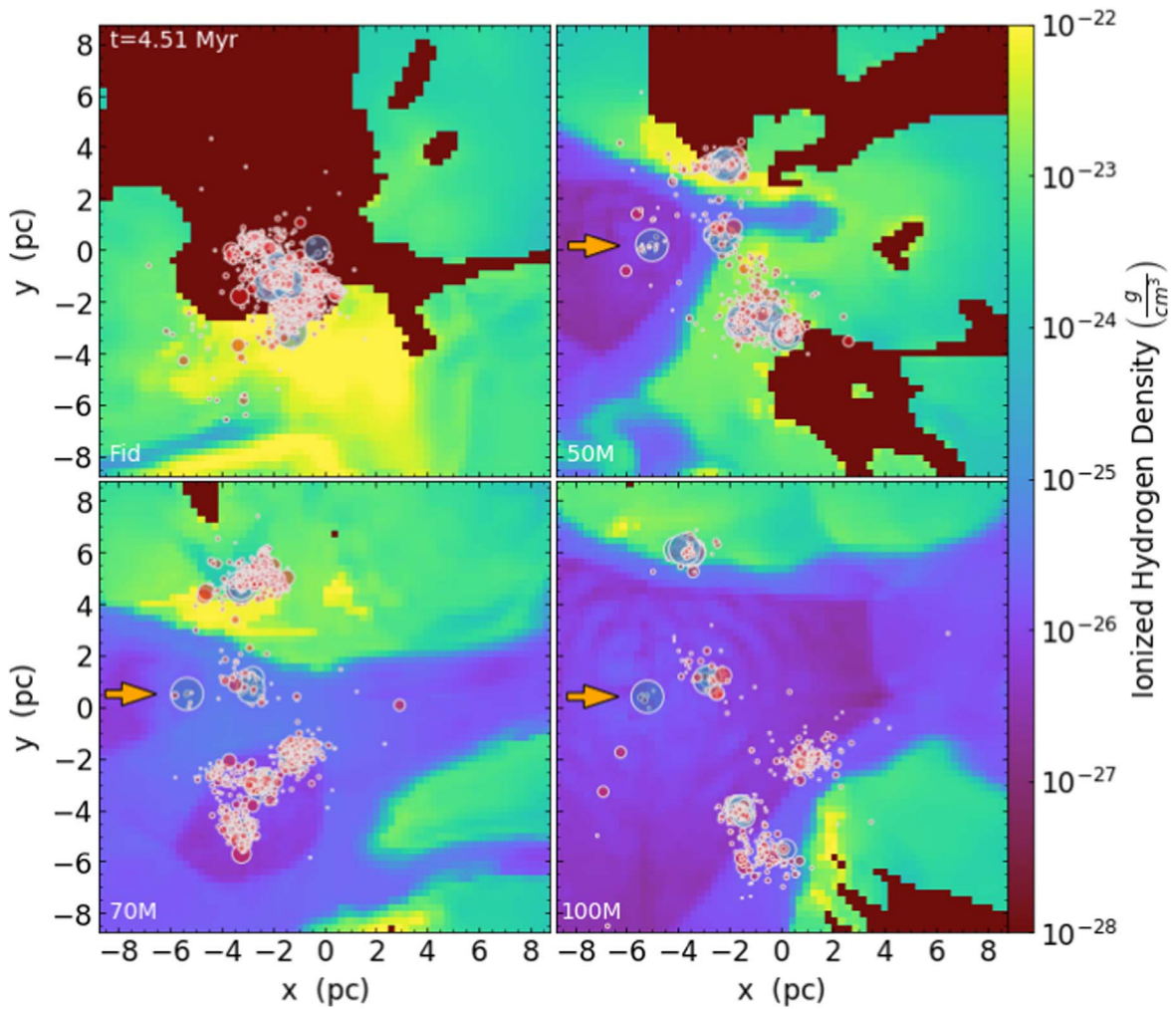


Figure 2. The same snapshot as in Figure 1 at $2\tau_{\text{ff}}$, but as a slice at $z = 0$ pc of the ionized Hydrogen density. To highlight the morphology of the ionized regions, a gas cell is determined to be fully ionized if its ionization fraction exceeds 0.99. Gas cells that do not meet this threshold do not have their densities represented and appear in the dark maroon color. The stars are shown, but note that they may lie above or below the plane of the slice. The orange arrows highlight the forced massive star in each of the forced runs.

of the gas on gas and the stars on gas. When the total energy becomes positive, the gas is in a globally unbound state. While this does not necessarily indicate that the natal GMC has been destroyed or will completely dissipate (as there could still be regions of gravitationally dominated gas that will continue to collapse and form stars), it does provide a metric for quantifying the global effects of the energy injection.

Figure 3 shows that the gas reaches a globally unbound state at 2.0–2.1 Myr after the simulation’s start for the forced runs, and at 3.9 Myr for the fiducial run. The transition to a globally unbound state of gas coincides with the formation of massive stars (1.8, 1.9, and 2.1 Myr for the 50, 70, and 100 M_{\odot} stars, respectively), while the fiducial transition occurs during a rapid formation of stars, including two stars with masses over 60 M_{\odot} .

The fiducial run also has a spike in energy a few hundred thousand years before its transition to a positive energy state. This initial spike is driven in part by the formation of a 29 M_{\odot} star several parsecs from the center of mass of the cloud, at $t = 2.51$ Myr. It remains the most massive star on the grid for the next million years. As the H II region around the star increases in volume, we see an increase in the total thermal energy of the gas in conjunction with a more slowly increasing total kinetic energy, produced by feedback from this star.

Around $t = 3.1$ Myr, several lower-mass feedback-producing stars (ranging from 12.49 to 17.24 M_{\odot}) form in the center of mass of the collapsing cloud. Their feedback, in addition to the influence of the 29 M_{\odot} star, results in the brief energy spike at $t = 3.5$ Myr. The total gas energy then declines rapidly, as more gas falls toward the gravitational center of the cloud and more stars are formed there. An off-center star such as this cannot markedly reduce the gas collapse by sweeping up large amounts of dense cold gas as the wind and ionization bubbles expand, unlike a star closer to the center of mass.

The gas total energy in the fiducial run finally becomes positive immediately following the formation of a 69.92 M_{\odot} star at 3.76 Myr, followed by a 49.86 M_{\odot} star at 3.85 Myr and a 62.96 M_{\odot} star at 3.96 Myr, along with two dozen other less massive feedback-injecting stars throughout the same time span.

The early-forming massive stars significantly accelerate the global unbinding of the available gas. The large spikes in energy at 5–6 Myr for the forced runs are due to the injection of Wolf–Rayet winds from the early-forming massive star and the subsequent supernova explosion. Since the early-forming massive stars drift significantly over their 4 Myr life spans, the supernovae occur near the edge of the computational

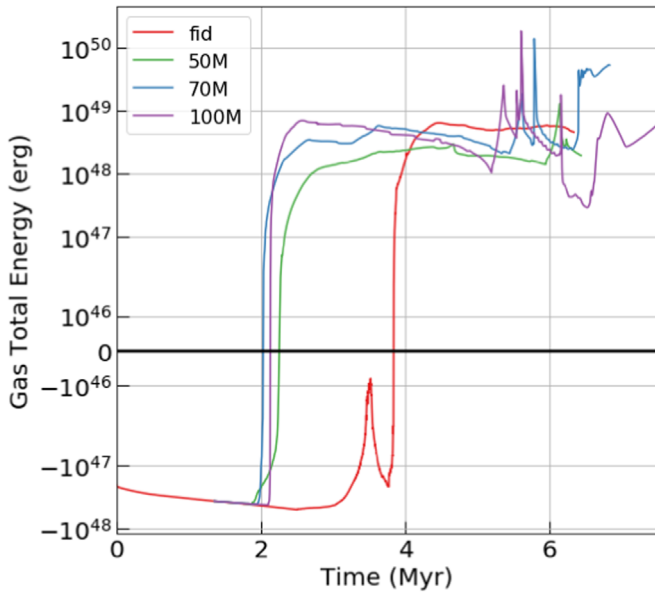


Figure 3. Total energy of the gas in the computational domain, comprising the kinetic, thermal, and magnetic energy of the gas, the energy from gas self-gravity, and the gravitational energy due to the stars acting on the gas, for the fiducial and forced runs. The y -axis is truncated close to zero, to reveal the details at times before and after the transition from negative to positive total energy. In each case, the energy is first dominated by the gravitational potential energy, then it becomes dominated by the gas kinetic energy and the gas thermal energy once the massive star forms in the forced runs or several $>50 M_{\odot}$ stars form in the fiducial run.

domain in the $50 M$ and $70 M$ runs, and the forced star in the $100 M$ run actually leaves the computational domain before going supernova. At the last simulation output, the most massive stars in the fiducial run are still 2–3 Myr away from these final stages of stellar evolution. Because of this, the global gas energy of the fiducial run fluctuates far less than in the final stages of the forced runs.

The left plot of Figure 4 shows that the total amount of the gas mass in the computational domain decreases most rapidly in the $70 M$ and $100 M$ runs. In each run, gas loss occurs due to expulsion from the computational domain or accretion onto sinks followed by conversion into stars. The right plot of Figure 4, which shows the cumulative ZAMS stellar mass placed on the grid, demonstrates that the majority of the decrease in the global gas mass in the $50 M$, $70 M$, and $100 M$ runs is due to gas expulsion from the grid. On the other hand, the fiducial run forms significantly more stars than the forced runs, and nearly the entirety of the decrease in gas mass before 4.5 Myr is due to the conversion of gas to stars. However, after $2\tau_{\text{ff}}$, nearly all of the subsequent decrease in the global gas mass is due to gas expulsion.

In both the $70 M$ and $100 M$ runs, the majority of the stars exit the computational domain by the end of the run. Interestingly, the $70 M$ run cumulatively forms $\sim 200 M_{\odot}$ less stellar material than the $100 M$ run. We do not investigate whether there are any unique mechanisms behind this, but instead focus on the significant discrepancy between the forced runs and the fiducial run.

The $50 M$ forced run was still actively forming stars at its end, even after the $50 M_{\odot}$ star had gone supernova. Although it had formed many fewer stars than the fiducial run, $2000 M_{\odot}$ of gas remained on the grid, so it still had the possibility of

forming enough stars to match the fiducial run. However, there are two reasons why it is unlikely that the remaining gas on the grid will produce any stars or subclusters that will interact with the stars on the grid at the time of our analysis. First, as can be seen in Figure 5, only 25% of the gas remaining on the grid in the $50 M$ model meets the Jeans instability criterion, one of the six that must be met to allow gas to be converted into star-forming sinks. Second, even if any of the unstable gas is able to form sinks that then accrete more gas to form stars, Figure 3 shows that the gas has positive total energy, so it is unlikely to collapse further. We further explore this reasoning in Section 3.3.

The fiducial, 70, and 100 M_{\odot} runs end with long periods without star formation. In the 70 and 100 M_{\odot} runs, nearly all of the initial gas has been exhausted, with only 10–20 M_{\odot} of hot gas remaining. The fiducial run has nearly all its stars and all its sinks remaining in the computational domain. In this case, the lack of growth of the total stellar mass is due to the sinks being concentrated at the stellar center of mass of the cloud, which becomes entirely devoid of gas following the formation of several high-mass stars during the rapid star formation event at 3.8 Myr. There is also a total of $1000 M_{\odot}$ of gas in the computational domain at the end of the run—none of it is gravitationally collapsing, so the star formation has ceased.

3.2. Sink Accretion and Star Formation

We show the rate of gas accretion onto all the sinks present on the grid, as well as the rate of star formation, in Figure 6. Accretion onto sinks requires the gas to be converging, bound to the sink, Jeans-unstable, and within the sink’s accretion radius. We expect the total accretion rates to fluctuate as more sinks form, as more gas flows into and onto the sink regions, and as massive stars—that heat or expel dense gas—form, preventing its accretion. Higher rates of accretion indicate lesser degrees of gas disruption by massive stars. Very low or zero accretion indicates that the gas in, on, and around the sinks has either been exhausted or has been disrupted by massive star feedback—heated so that it is no longer Jeans-unstable or expelled from the sink accretion zones. The red line in Figure 6 tracks the global star formation rate (SFR). We calculate the SFR by taking the derivative of a spline fit that has been applied to the cumulative stellar mass. We then smooth the results using a moving-median filter with a 100 kyr window size, to avoid effects due to overfitting.

Interestingly, the fiducial, $50 M$, and $100 M$ runs have distinct peaked accretion rates at ~ 4 Myr (see Figure 6), which similarly decrease for the next megayear or so. The fiducial peak is an order of magnitude higher than the median accretion rate of the forced runs, as clearly represented in the cumulative stellar mass that is formed, as shown in Figure 4. The violent accretion event in the fiducial run was able to produce enough massive stars to terminate all further accretion in the computational domain. The forced massive stars are able to stifle sink accretion in the time immediately after their formation at ~ 2 Myr (as seen most prominently in the $50 M$ and $70 M$ runs). At 3 Myr, as the outer regions of the cloud continue to collapse, the accretion rates of the forced runs are able to recover to levels similar to that of the fiducial run at the equivalent time, but the forced runs never experience a similarly rapid gas accretion event. Gas accretion also continues for much longer in the forced runs than in the fiducial run. The SFR diverges from the sink accretion rate at

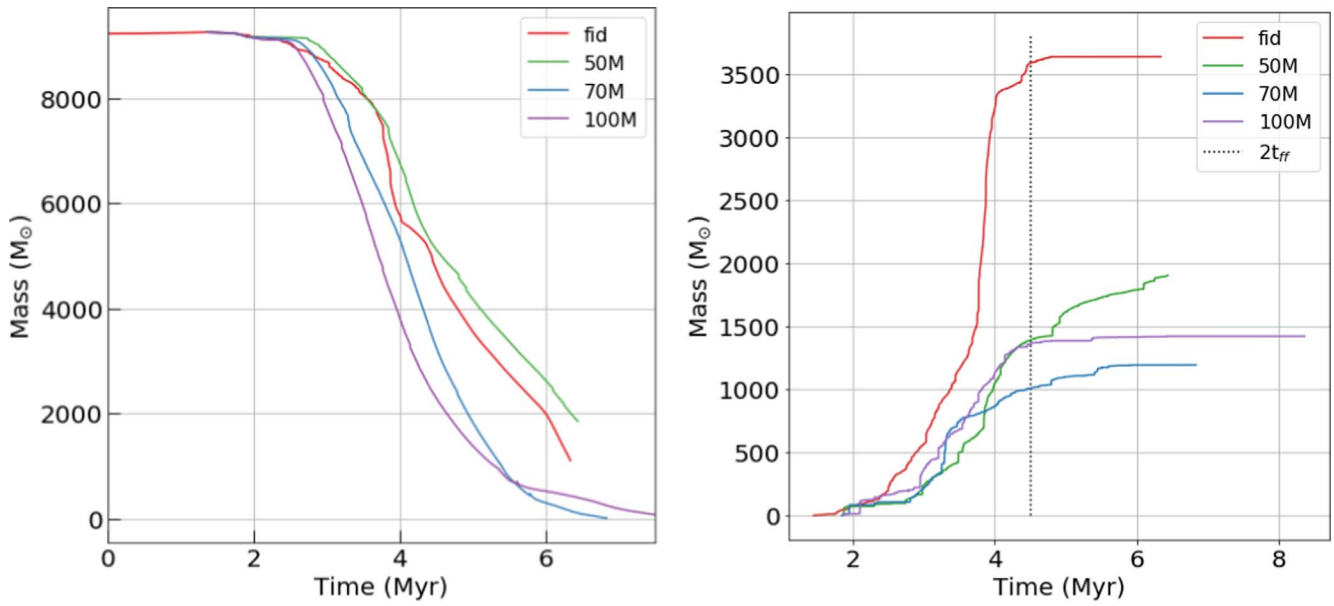


Figure 4. Left: total gas mass in the computational domain. The reduction in gas is due to gas leaving the domain or accreting onto sinks and ultimately becoming stars. Right: the cumulative ZAMS stellar mass for the fiducial and the three forced massive star runs. The dotted vertical line marks $2t_{ff}$, the focus of Section 3.3.

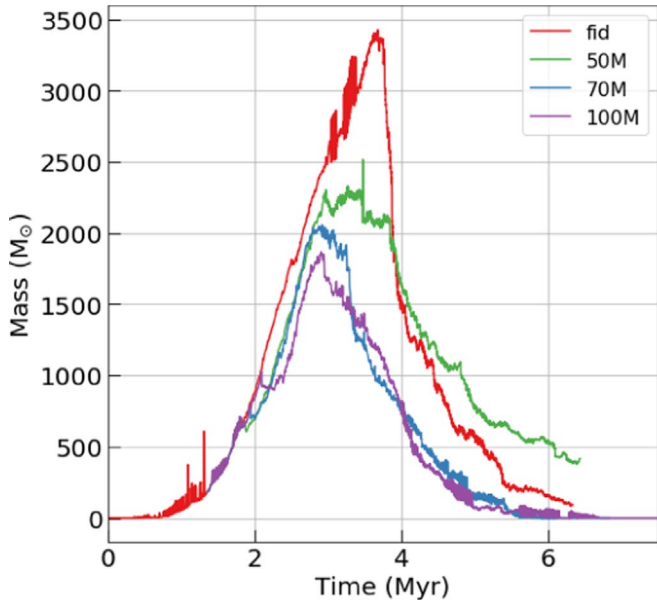


Figure 5. Total mass of the gas in the computational domain that satisfies the Jeans criterion, one of the six criteria necessary for sinks to form, and one of four sink accretion criteria.

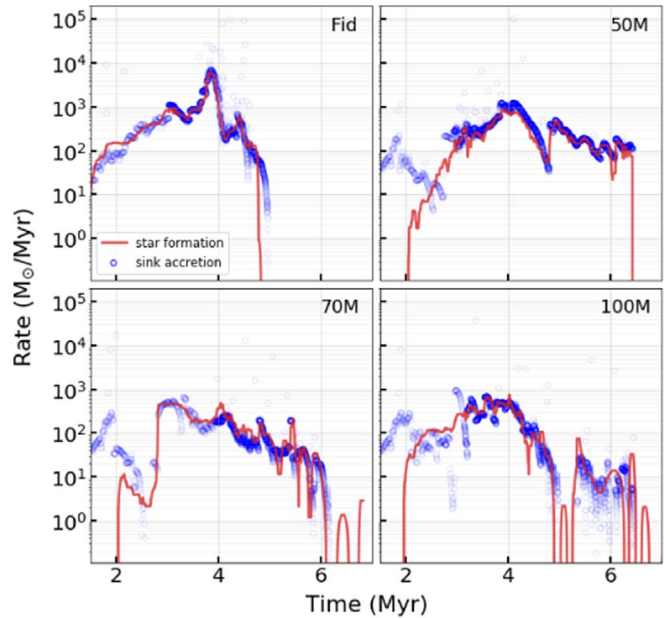


Figure 6. Global sink accretion rates (blue circles) and SFRs (red lines) for each run. The SFR lines are smoothed with a 100 kyr windowed median, to correct for the effects of taking the derivative of the spline fit.

early times in the forced runs, because the early-forming massive star only allows its parent sink to accrete gas until the star forms. Once the massive star forms, and as more sinks form, the SFR closely tracks the sink accretion rate and shows similar trends.

Some significant outliers in the sink accretion data can be seen. These correspond to the accretion of large masses of gas onto a single sink. A sink can move to a nearby region of very dense gas that was previously beyond the sink’s accretion radius. If the gas, now within the accretion radius, satisfies all the accretion criteria, a large mass of gas accretes in a single time step, also resulting in high accretion rates. This behavior is not unexpected, and is easily explained by the movement of sinks onto particularly dense cells of readily accreting gas,

although 0.1% of the GMC’s initial mass being accreted in a single time step can likely be further resolved with a more refined grid structure that allows for more detailed accretion events.

We require the volume within the sink accretion radius to be cold gas with $T < 100$ K in order for the sink to form stars. This choice has been made because we sample each newly born star’s relative velocity from the sound speed of the gas in the sink volume. If the gas were to be too hot, the stars would be placed with unrealistic relative velocities. Because of this requirement, it is possible for sinks to accrete gas, but not to form stars, if the region within the sink radius is heated by stellar feedback. Such an effect can be seen at the end of the fiducial run, when the SFR diverges from the sink accretion

rate (see Figure 6). This model can have the undesirable effect of trapping gas within a sink until it ventures into a region of cold gas. Improved models—preventing sink accretion if star placement is forbidden—have been proposed and will be implemented in future versions of TORCH.

In each of the simulations, there are five sinks present at $2\tau_{\text{ff}}$. In the 50 M run, 110 M_{\odot} of gas is trapped within these sinks, the most massive of which contains the majority of the mass, at 96 M_{\odot} . The 70 M run has 22 M_{\odot} trapped, with the most massive sink containing 17 M_{\odot} . The 100 M run has just over 3 M_{\odot} of trapped gas, with 2.5 M_{\odot} in the most massive sink. The fiducial run has a total of 19 M_{\odot} trapped in its sinks, with 18 M_{\odot} in the most massive one.

The SFE per freefall time is

$$\epsilon_{\text{ff}} = \dot{M}_{*} \frac{t_{\text{ff}}}{M_{\text{g}}}, \quad (1)$$

where \dot{M}_{*} is the instantaneous SFR, t_{ff} is the cloud’s initial freefall time, and M_{g} is the remaining gas mass. Averaged over the star formation time, ϵ_{ff} has values of 0.23, 0.08, 0.03, and 0.04 for the fiducial, 50 M , 70 M , and 100 M runs, respectively. These results are consistent with the observed values (as collected and reported by Krumholz et al. 2019). The high SFE of the fiducial run is likely due to the low virial ratio of the initial cloud, which promotes a more aggressive conversion of gas to stars. It is also worth noting that our model assumes 100% SFE for the gas that a sink accretes, which may result in a higher overall SFE. In addition, our model does not yet include protostellar jets, with disruptive feedback effects that would lower the SFE (Federrath 2015; Appel et al. 2022). The early massive star formation in our simulations significantly disrupts the early gas accretion and prolongs the star formation history of a cloud, but at the cost of stifled sink accretion rates, as well as greatly reduced SFRs and average formation efficiencies per freefall time.

3.3. Cluster Properties

We identify stellar clusters at $2\tau_{\text{ff}}$ and examine their properties to demonstrate the impact of early massive star formation on the clusters (see Figure 7). We choose this characteristic time to perform our clustering analysis because some star clusters leave the domain later in the simulations.

3.3.1. Cluster Identification

We use DBSCAN from the `scikit-learn` Python library (Pedregosa 2011) to identify the clusters, following Wall et al. (2020). DBSCAN identifies clusters as collections of core and boundary particles. We choose the core particles to be stars that have at least 12 neighbors within 0.66 pc, while the boundary particles lie within 0.66 pc of a core particle, but have fewer than 12 neighbors. Our parameters are slightly more restrictive than those used in Wall et al. (2020): we set the outer density limit for the maximum distance calculation as $2.0 M_{\odot}/\text{pc}^3$, rather than $1.0 M_{\odot}/\text{pc}^3$, to better separate the clusters from the more sparse field stars, as well as to promote the separate identification of two nearby clusters whereas a less restrictive model would only identify one.

It is important to note that DBSCAN only groups stars into clusters based on their spatial proximity to one another, and that it does not consider any dynamical or energetic properties

of the cluster members. In order to include some energetic information as part of the cluster identification process, we check whether each cluster member is bound to the center of mass of its parent cluster. If the fraction of unbound stars in a single cluster exceeds 50%, and the cluster has a mass of less than 100 M_{\odot} , we reject the cluster. This restriction operates as a way of systematically cleaning up the tendency of DBSCAN to identify collections of field stars as clusters, despite the members being spatially and energetically separate.

Once the clusters have been identified, we determine the half-mass radius r_{h} , to give a sense of the compactness of each of them. We also record the mass of each cluster, as well as the fraction of the total mass that the cluster constitutes, compared to the total mass of all the stars formed in the simulation at this point.

The fragmenting of the cloud in the forced early massive star runs promotes the formation of distinct star clusters that move toward the edge and eventually out of the computational domain. Indeed, in the 100 M run, all star clusters leave the computational domain by the end of the simulation. These distinct clusters in the forced runs seem to track the escaping gas, and would likely not fall together in a collapse event, as we discuss further in Section 4.1.

3.3.2. Cluster Properties

Figure 7 shows that the fiducial run results in a relatively compact single cluster, which represents over a third of all the initially available gas mass as well as 99% of the stars that have formed in the simulation. This is in stark contrast to each of the early-forming massive star runs, in which stellar material is broadly distributed across multiple spatially separated stellar associations, despite the systems being the same age and deriving from identical initial conditions.

The fraction of the mass contained within the clusters also indicates the increasing levels of disruption in cluster assembly in the early-forming massive star runs. In the 50 M run, 97% of all the stellar mass is contained within the four identified clusters. In the 70 M run, the mass fraction is slightly lower, at 85%. In the 100 M run, only 46% of the stellar mass is contained within the identified clusters, meaning that over half of all the stars formed in the run are in very loosely bound associations, are lone field stars, or have left the computational domain. The 100 M run has the most clusters rejected for insufficient mass or gravitational boundness, with three, each of which can be picked out by eye in Figure 7, as the collections of gray points. The 70 M and 50 M runs both have a single cluster rejected. The clusters in the early-forming massive star runs are significantly less massive than the single cluster in the fiducial run, as expected, since the fiducial run forms two to three times as much stellar material.

The half-mass radii included in Figure 7 show the relative compactness of the clusters. We calculate r_{h} from the center of mass of each cluster, excluding any gas that may be present within the cluster region. The single cluster in the fiducial run is compact, with half of its mass within 0.25 pc of the center of mass, despite its outermost stars extending up to 2 pc away. Interestingly, the most massive clusters in each of the early-forming massive star runs (the blue clusters in each of the cases) have the smallest values of r_{h} , at 0.17, 0.21, and 0.18 pc for the 50 M , 70 M , and 100 M runs, respectively.

We also calculate the boundness between the centers of masses of all the clusters to the most massive cluster on the

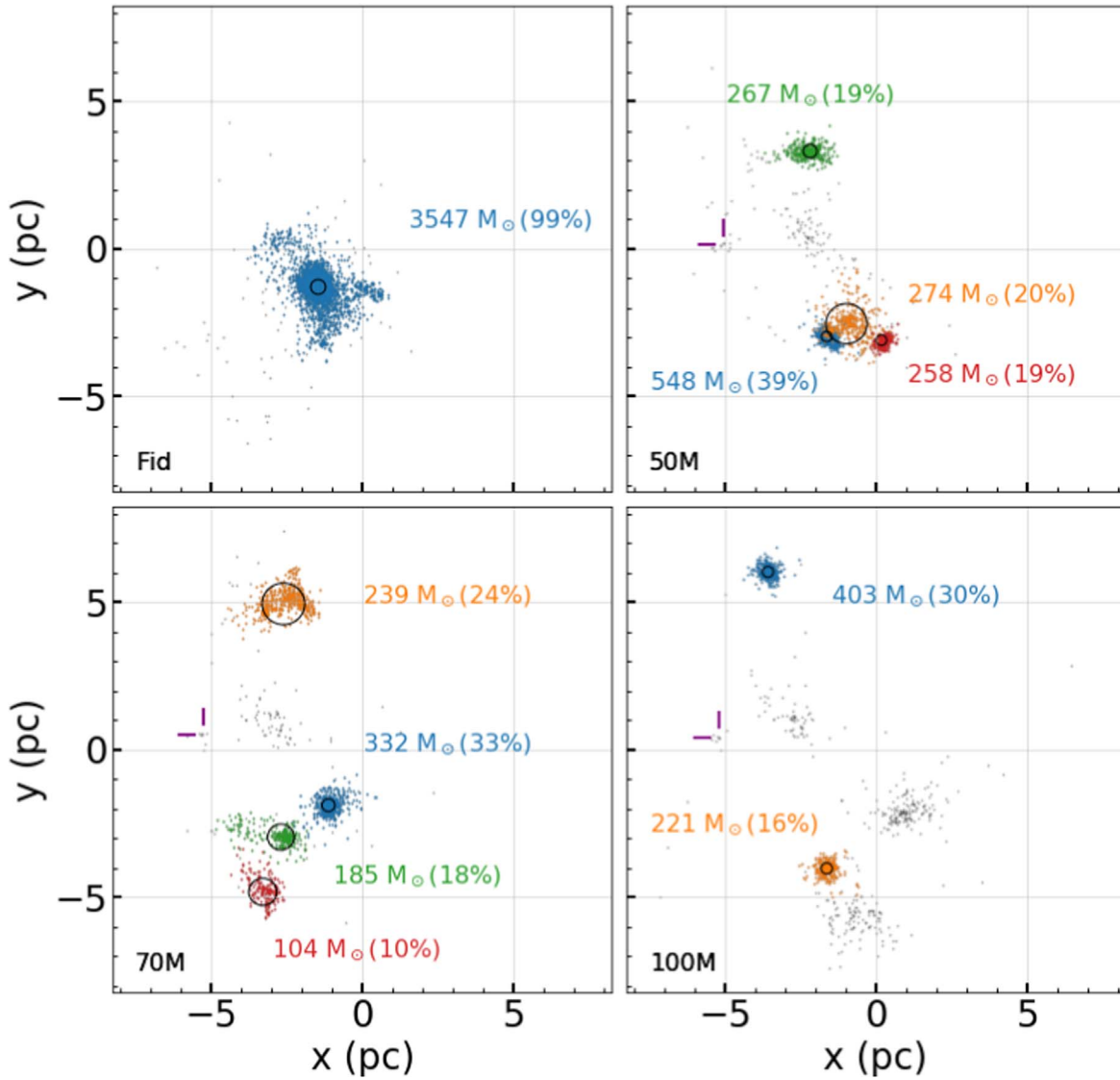


Figure 7. Snapshot of the star clusters formed in the fiducial and forced runs at $2\tau_{\text{ff}}$. The clusters are identified using DBSCAN. Each cluster is labeled with color-coded text giving the cluster total mass and the mass fraction of all the formed stars contained within the cluster. Overlaid on each cluster is its half-mass radius. In each of the forced runs, the early-forming massive star does not belong to an identified cluster. Stars that are not members of clusters are shown by the gray points. The position of the early-forming massive star is indicated with the purple crosshairs.

grid. In the $50 M$ run, only the least massive identified cluster (red) is bound to the most massive cluster. In the $70 M$ and $100 M$ runs, the centers of masses of all the identified clusters are unbound relative to the most massive cluster. In the fiducial run, portions of the cluster break into two smaller subclusters, of less than $100 M_{\odot}$, at later times, but the centers of masses of those subclusters remain bound to the main fiducial cluster center of mass. The clusters formed in this work are more compact and lower in mass than the older clusters observed by Kharchenko et al. (2013). However, they are consistent with the six deeply embedded clusters observed by Kuhn et al. (2014). A summary of the cluster comparison data is collected in Table 1.

In each run, the early-forming massive star is not associated with any cluster. This is not unusual, since the star is able to rapidly drive away gas from its parent sink, so that no subsequent star or cluster formation can occur in the massive star’s vicinity. In addition, the rapid removal of gas from the

Table 1
Cluster Statistics at $2\tau_{\text{ff}}$

Run	# of Clusters ^a	Mass of Clusters ^b $10^3 M_{\odot}$	Frac Mass ^c M_c/M_{tot}	r_h MMC ^d pc	E_{bind} MMC ^e 10^{46} erg
Fid	1	3.6	0.99	0.25	-140
$50 M$	4	1.4	0.97	0.17	-12
$70 M$	4	0.86	0.85	0.21	-4.2
$100 M$	2	0.62	0.46	0.18	-3.8

Notes.

^a The number of clusters on the grid, as identified by DBSCAN, that pass the mass and boundness criteria.

^b The stellar mass contained within all of the identified clusters.

^c The fraction of stellar material present in all of the clusters relative to the total cumulative mass of the stars that have formed.

^d The half-mass radius of the most massive cluster (MMC).

^e The binding energy of the MMC.

center of the cloud allows the early-forming massive star and its parent sink to drift out of the cloud center, since the gas gravitational potential is so severely disrupted. In the fiducial run, at $2\tau_{\text{ff}}$, 10 very massive stars with $M > 20 M_{\odot}$ are present in the identified cluster, including 49, 61, and $67 M_{\odot}$ stars. Of these, seven reside within r_{h} , and six of those are within the 12.5% mass–radius relation, at just 0.084 pc. In the forced runs, the identified clusters have few or no stars with $M > 20 M_{\odot}$, which is to be expected when considering the random sampling of the Kroupa distribution (Weidner & Kroupa 2006) of clusters with low total mass.

We also analyze the most massive star in each cluster, by finding the ratio of its mass to the approximate maximum stellar mass relation proposed by Larson (2003): $M_{\text{star}} \sim 1.2M_{\text{cluster}}^{0.45}$. The fiducial run has a ratio of 1.41, and the most massive star in the identified cluster is 1.41 times the Larson (2003) relation. The four clusters in the 50 M run have ratios of 0.65, 2.98, 1.56, and 1.45, in order of descending total cluster mass. The maximum mass relations of the 70 M clusters run are 1.87, 1.83, 4.60, and 1.07. The 100 M ratios are 1.06 and 1.17. In order to include the field stars that are not within identified clusters, we also take the ratio of the most massive star in the computational domain to the Larson (2003) relation, using the sum of all stars as M_{cluster} . The ratios for the fiducial, 50 M , 70 M , and 100 M runs are 1.28, 1.40, 2.16, and 0.74. This similarity between the fiducial and forced runs is expected, as each sink is assigned its own mass list, from which the stars are formed. A massive star that is forced to form early from one sink will not have a direct effect on the star masses that are formed by sinks elsewhere in the GMC. Overall, early-forming massive stars do not cause individual clusters or the entire star field to diverge from the Larson (2003) relation.

In the fiducial run, the location and compactness of the distribution of massive stars is likely a result of early mass segregation (Binney & Tremaine 1987; McMillan et al. 2007). We find that stars with $M > 3M_{\odot}$ have $r_{\text{h}} = 0.207$ pc, while for all stars, $r_{\text{h}} = 0.247$ pc (excluding the $\sim 67M_{\odot}$ star several parsecs from the cluster center of mass yields $r_{\text{h}} = 0.165$ pc for heavy stars).

4. Discussion

4.1. Previous Work

The suppression of the global SFR and the fragmentation of the initial GMC seen in our forced runs have been observed in other simulations, although under different circumstances. Chen et al. (2021) found that variations in the initial gas density distribution of the GMC resulted in two modes of star cluster formation. GMCs with steep power-law density distributions form a single massive cluster, growing via direct gas accretion, similar to the cluster formed in our fiducial run. Nearly all of the mass in the fiducial cluster is due to star formation, via its central sinks, rather than through merger events with subclusters. GMCs with top-hat gas distributions and otherwise identical properties fragmented into stellar subclusters, similar to our forced massive runs. However, Chen et al. (2021) observed these subclusters assembling hierarchically into central clusters, while we do not see significant evidence for hierarchical assembly in our forced massive star runs. The similar subcluster formation is likely due to the forced massive star forming very near to the density center of

our GMC. The destructive effect of the stellar feedback occurring so early in the collapse of the cloud redistributes a significant portion of the GMC’s initial mass to the outer sections of the cloud. The feedback acts as a source of internal pressure, preventing the gas from collapsing into the gravitational center, with the result that it fragments into smaller, spatially distributed subclusters instead.

Similar to Dale et al. (2014), we find that winds and the ionizing feedback of deeply embedded massive stars disrupt the natal gas cloud. Our results also agree with the destruction of natal gas clouds found in the 1D model WARPFIELD (Rahner et al. 2019) and with the destructive effects reported in previous Torch simulations in which a very massive star forms (Wall et al. 2020).

In one of the simulations detailed in Wall et al. (2020), a $\sim 97 M_{\odot}$ star was born around 1.5 Myr after the onset of star formation in the main cluster. Its formation rapidly expelled gas from the cluster, halting local star formation and causing the least bound members of the cluster to be lost, but ultimately leaving the cluster intact. Similar results are exhibited in our fiducial run.

Our random stellar mass sampling technique mirrors the suggestion from Weidner & Kroupa (2006) for producing a realistic IMF. A consequence of this technique is the trend to a stellar mass threshold, which depends on the total mass of the star cluster (Larson 2003). While our early-forming massive stars obviously diverge from the intended prescription, our desire is to probe the anomalous yet possible scenario that such a random sampling technique could produce very massive stars very early in the star formation history of a cluster. Still, our clusters adhere relatively well to the Larson (2003) approximate maximum stellar mass relation. Comparing the most massive stars in each cluster, seven of 11 are within a factor of 1.6 of the Larson (2003) relation (see Section 3.1). Though there are clusters with divergent ratios, it should be noted that these values are based on a snapshot of the clusters at $2\tau_{\text{ff}}$, and so are subject to change, as the clusters dynamically evolve and the massive stars shed mass as stellar winds.

4.2. Limitations

The initial conditions used in our runs are simplified, to best test our hypothesis and also to streamline the initialization of the simulations as much as possible. Our turbulent spherical cloud neglects any of the complex dynamical interactions that GMCs encounter in their precollapse phase, including galactic potential. Hence, we do not resolve any tidal effects that the cloud may experience. Since the cloud only evolves for 2 Myr prior to star formation, though, we assume the tidal effects resulting from orbiting a galaxy to be negligible. We also start with a rather low virial parameter of 0.12 (with 0.5 being equilibrium). This low virial parameter effectively assumes an evolutionary history of global gravitational instability or galactic-scale collision at a scale larger than our simulations.

Our model does not include pre-main-sequence feedback effects, such as jets or accretion luminosity, which would act during the main accretion phase. If we were to resolve the subgrid dynamics of stellar accretion, we would expect the destructive effects of the forced massive stars to turn on even earlier, to account for the star’s pre-main-sequence evolution, eventually reaching the ZAMS feedback that we see in our runs. The inclusion of instantaneous ZAMS feedback in our forced massive star runs results in the high likelihood of the

forced massive star remaining unassociated with a cluster, as its feedback immediately prevents its parent sink from forming any other stars. It is also possible that the pre-main-sequence feedback could further disrupt the hierarchical assembly process of the cluster and better halt the collapse of the initial cloud. That being said, the massive star pre-main-sequence evolution is very fast, with the main accretion phase only lasting about 10^5 yr (e.g., Palla & Stahler 1999). Indeed, our forced massive stars take only a few hundred thousand years to form from their parent sinks. Furthermore, the vast majority of the energy input from the forced massive stars occurs during their main-sequence and post-main-sequence evolution.

The process through which massive stars form remains under debate (Tan et al. 2014; Krumholz 2015; Motte et al. 2018). Our models cannot resolve the formation of individual massive stars. Instead, we use a subgrid star formation model. This model identifies a region of gas that will continue to collapse, allows accretion into the region, and then forms stars chosen from the Kroupa IMF. Since we only model accretion into star-forming regions at large scales of 0.5 pc, we remain agnostic to ongoing debates about the formation of individual stars, such as the importance of fragmentation-induced starvation (Peters et al. 2010) or monolithic collapse (McKee & Tan 2003). Ultimately, our ability to form stars one by one, to track their feedback, nuclear evolution, and dynamics, allows us to probe the effects of massive stars on an actively forming star cluster. Also, the abnormally large mass of our early-forming massive stars may be unlikely to appear in reality, but within our computational model, the sink is able to accrete enough gas to justify such a star. Forcing a massive star to form early probes the extremes of what may be possible in a `Torch` simulation. Also, massive stars preferentially form in multiples (Duchêne & Kraus 2013). While this work does not include primordial binaries, Cournoyer-Cloutier et al. (2021) have successfully implemented a primordial binary model within `Torch` that will be included in future work. That said, Cournoyer-Cloutier et al. (2023) find that the early dynamical evolution of low-mass clusters is not dominated by two- or few-body interactions, but by the gravitational potential of the star-forming region.

Higher resolution would affect how the gas is accreted onto sinks, how the stars are placed, and how the stars interact with the gas. Higher maximum levels of refinement would require smaller sinks to form, with smaller accretion and star placement regions, but would also capture more details of the massive star feedback interactions with gas. If one of our sinks is accreting material for a massive star on the list, no low-mass star formation is allowed within its accretion radius. Higher grid refinement and smaller sinks could separate a region of dense gas into multiple star formation regions, allowing other stars to form while one of the sinks remains in the accretion stage. That said, once a very massive star is born, the effects on its surroundings are similar in both low- and high-resolution runs. Feedback from massive stars will suppress the star formation and expel gas even in simulations with higher maximum refinement levels.

Last, a significant fraction of the gas is ejected from the computational domain. This gas could recollapse, allowing for further star formation, if it leaves the computational domain with insufficient speed to escape the newly formed star cluster. Using the results from the 1D model `WARPFIELD` (Rahner et al. 2018), we can check this possibility, by examining the SFE and peak cloud density. Our runs have total SFEs of

0.13–0.39 and an initial peak cloud number density of 525 cm^{-3} . These values exclude the possibility of a recollapse event occurring. We therefore assume that the gas that exits the computational domain will not recollapse into the star-forming region, and that it may be completely dispersed by later stellar feedback. The stars that form within our computational domain will continue to remain isolated from any gas that is ejected from the system, as well as from any potential star formation that could occur in that gas.

5. Conclusion

Using runs with identical initial conditions, but different times of formation for the first massive stars, we find that early-forming massive stars:

1. globally unbind gas nearly 2 Myr earlier than our fiducial run;
2. reduce the global SFE by up to a factor of 3 and the average SFE per freefall time by up to a factor of 7;
3. promote the formation of isolated stellar subclusters; and
4. hinder the subclusters from collapsing into a single massive cluster.

The early-forming massive stars significantly disrupt the natal gas environment, globally unbinding gas nearly 2 Myr earlier than our fiducial run, which lacks the early formation of a massive star. As a result, the massive stellar feedback evacuates the gas from the computational domain more rapidly in the runs with an early massive star, thus dramatically reducing the amount of star formation. While the gas in the fiducial run remains more centrally concentrated than in the runs with early-forming massive stars, and the gas accretion rate onto sinks leading to the formation of stars is up to an order of magnitude higher, the star formation in the fiducial run is still entirely quenched by around twice the freefall time of the initial cloud, about 3 Myr after the onset of star formation. This termination of star formation occurs because of the global unbinding of the gas by feedback from later-forming massive stars.

In the early massive star runs, star formation still occurs for several million years after the gas reaches a globally unbound state. This is indicative of isolated subcluster formation, where small separated pockets of gas can continue to collapse and form stars, even after most of the gas has been expelled. Of the three early massive star runs, the 100 M and 70 M runs expel more gas from the computational domain, produce and maintain less Jeans-unstable gas, and ultimately form fewer stars than the 50 M run. This trend is also seen in the comparison between the 50 M and fiducial runs.

Before the star formation is quenched in the fiducial run, around one-third of the initial gas is converted to stars, two to three times more than in the early massive star runs. We also find that early-forming massive stars cause star formation to occur in spatially separate and energetically unbound subclusters. In the fiducial run, in contrast, a single star cluster, containing nearly all the stars, forms. At the same simulation time, the early massive star runs all have several clusters present, but fewer stars associated with the clusters, with the 100 M run having less than half of all the formed stars present in the two identified clusters. The most massive clusters in the early runs at $2\tau_{\text{ff}}$ contain less than 40% of the total stars formed, and have masses of only a few hundred solar masses, while the fiducial cluster has a mass of $3500 M_{\odot}$. Although

there will likely be a little more star formation occurring in the early runs, as expelled gas continues to collapse outside the computational domain, any last stars that are formed will likely not be associated with a larger single cluster, and the gas will not be likely to recollapse to trigger a second round of star formation at the center of the cluster. Early-forming massive stars, in otherwise identical initial gas clouds, greatly disrupt the gas collapse, star formation, and cluster assembly processes.

We acknowledge useful discussions of the stellar evolution code `SeBa` with S. Toonen. M.-M.M.L., S.L.W.M., and A.T. were partly supported by NSF grant No. AST18-15461. S.L.W.M. was also supported by NSF grant No. AST18-14772. A.T. was also supported through a NASA Cooperative Agreement awarded to the New York Space Grant Consortium. A.S. and C.C.-C. are supported by the Natural Sciences and Engineering Research Council of Canada. C.C.-C. also acknowledges funding from a Queen Elizabeth II Graduate Scholarship in Science and Technology (QEII-GSST). M.W. is supported by NOVA, under project No. 10.2.5.12. B.P. thanks the International Max Planck Research School for Astronomy and Cosmic Physics at the University of Heidelberg (IMPRS-HD) for their financial support. R.S.K. acknowledges support from the European Research Council via the ERC Synergy Grant “ECOGAL” (project ID 855130), from the Heidelberg Cluster of Excellence (EXC 2181-390900948) “STRUCTURES,” funded by the German Excellence Strategy, from the German Research Foundation (DFG), in the Collaborative Research Center SFB 881 “The Milky Way System” (funding ID 138713538; subprojects A1, B1, B2, and B8), and from the German Ministry for Economic Affairs and Climate Action, in the project “MAINN” (funding ID 50002206). The Heidelberg group also acknowledges HPC resources and data storage supported by the Ministry of Science, Research and the Arts of the State of Baden-Württemberg (MWK) and DFG, through grant Nos. INST 35/1314-1 FUGG and INST 35/1503-1 FUGG, and computing time from the Leibniz Computing Center (LRZ), in project pr74nu. The simulations reported here were conducted on Cartesius; we acknowledge the Dutch National Supercomputing Center SURF grant No. 15520. M.-M.M.L. thanks the Institut für Theoretische Astrophysik for hospitality during work on this paper.




Facility: Cartesius; SURF—Dutch National Supercomputing Center.









Software: `Torch` (Wall et al. 2019, 2020), `AMUSE` (Portegies Zwart et al. 2009; Pelupessy et al. 2013; Portegies Zwart et al. 2013; Portegies Zwart & McMillan 2018), `FLASH` (Fryxell et al. 2000), `yt` (Turk et al. 2011), `numpy` (Oliphant 2007), `scikit-learn` (Pedregosa 2011), `matplotlib` (Hunter 2007), `HDF` (Koranne 2011).

Data Availability

The data from the simulations and figures within this article will be shared on reasonable request to the corresponding author.

ORCID iDs

Sean C. Lewis  <https://orcid.org/0000-0003-4866-9136>
 Stephen L. W. McMillan  <https://orcid.org/0000-0001-9104-9675>
 Mordecai-Mark Mac Low  <https://orcid.org/0000-0003-0064-4060>

Claude Cournoyer-Cloutier  <https://orcid.org/0000-0002-6116-1014>
 Brooke Polak  <https://orcid.org/0000-0001-5972-137X>
 Martijn J. C. Wilhelm  <https://orcid.org/0000-0002-3001-9461>
 Aaron Tran  <https://orcid.org/0000-0003-3483-4890>
 Alison Sills  <https://orcid.org/0000-0003-3551-5090>
 Simon Portegies Zwart  <https://orcid.org/0000-0001-5839-0302>
 Ralf S. Klessen  <https://orcid.org/0000-0002-0560-3172>
 Joshua E. Wall  <https://orcid.org/0000-0003-2128-1932>

References

- Appel, S. M., Burkhardt, B., Semenov, V. A., Federrath, C., & Rosen, A. L. 2022, *ApJ*, 927, 75
- Baczynski, C., Glover, S. C. O., & Klessen, R. S. 2015, *MNRAS*, 454, 380
- Banerjee, S., & Kroupa, P. 2017, *A&A*, 597, A28
- Bate, M. R., Bonnell, I. A., & Price, N. M. 1995, *MNRAS*, 277, 362
- Binney, J., & Tremaine, S. 1987, *Galactic dynamics* (Princeton NJ: Princeton Univ. Press)
- Bressert, E., Bastian, N., Gutermuth, R., et al. 2010, *MNRAS*, 409, L54
- Chen, Y., Li, H., & Vogelsberger, M. 2021, *MNRAS*, 502, 6157
- Chevanche, M., Kruijssen, J. M. D., Vazquez-Semadeni, E., et al. 2020, *SSRv*, 216, 50
- Chevanche, M., Krumholz, M. R., McLeod, A. F., et al. 2022, arXiv:2203.09570
- Colella, P., & Woodward, P. R. 1984, *JCoPh*, 54, 174
- Cournoyer-Cloutier, C., Sills, A., Harris, W. E., et al. 2023, *MNRAS*, submitted
- Cournoyer-Cloutier, C., Tran, A., Lewis, S., et al. 2021, *MNRAS*, 501, 4464
- Dale, J. E. 2015, *NewAR*, 68, 1
- Dale, J. E., Ercolano, B., & Bonnell, I. A. 2012, *MNRAS*, 424, 377
- Dale, J. E., Ngoumou, J., Ercolano, B., & Bonnell, I. A. 2014, *MNRAS*, 442, 694
- Dobbs, C. L., Bending, T. J. R., Pettitt, A. R., & Bate, M. R. 2022, *MNRAS*, 509, 954
- Dobbs, C. L., Liow, K. Y., & Rieder, S. 2020, *MNRAS*, 496, L1
- Draine, B. T. 1978, *ApJS*, 36, 595
- Duchêne, G., & Kraus, A. 2013, *ARA&A*, 51, 269
- Einfeldt, B., Munz, C. D., Roe, P. L., & Sjogreen, B. 1991, *JCoPh*, 92, 273
- Federrath, C. 2015, *MNRAS*, 450, 4035
- Federrath, C., Banerjee, R., Clark, P. C., & Klessen, R. S. 2010, *ApJ*, 713, 269
- Fryxell, B., Olson, K., Ricker, P., et al. 2000, *ApJS*, 131, 273
- Fujii, M., Iwasawa, M., Funato, Y., & Makino, J. 2007, *PASJ*, 59, 1095
- Gavagnin, E., Bleuler, A., Rosdahl, J., & Teyssier, R. 2017, *MNRAS*, 472, 4155
- Girichidis, P., Offner, S. S. R., Kritsuk, A. G., et al. 2020, *SSRv*, 216, 68
- Godunov, S. K., & Bohachevsky, I. 1959, *Mat. Sb.*, 47(89), 271, <https://hal.science/hal-01620642>
- Gouliermis, D. A., Elmegreen, B. G., Elmegreen, D. M., et al. 2017, *MNRAS*, 468, 509
- Grudić, M. Y., Guszejnov, D., Hopkins, P. F., et al. 2018, *MNRAS*, 481, 688
- Grudić, M. Y., Guszejnov, D., Hopkins, P. F., Offner, S. S. R., & Faucher-Giguere, C.-A. 2021, *MNRAS*, 506, 2199
- Guszejnov, D., Markey, C., Offner, S. S. R., et al. 2022, *MNRAS*, 515, 167
- Habing, H. J. 1968, *BAN*, 19, 421
- Heger, A., Fryer, C. L., Woosley, S. E., Langer, N., & Hartmann, D. H. 2003, *ApJ*, 591, 288
- Howard, C. S., Pudritz, R. E., & Harris, W. E. 2018, *NatAs*, 2, 725
- Hunter, J. D. 2007, *CSE*, 9, 90
- Hut, P., Makino, J., & McMillan, S. 1995, *ApJL*, 443, L93
- Kauffmann, J., Pillai, T., & Goldsmith, P. F. 2013, *ApJ*, 779, 185
- Kharchenko, N. V., Piskunov, A. E., Schilbach, E., Röser, S., & Scholz, R.-D. 2013, *A&A*, 558, A53
- Klessen, R. S., Glover, S. C. O., et al. 2016, *Saas-Fee Advanced Course*, 43, 85
- Klessen, R. S., Heitsch, F., & Mac Low, M.-M. 2000, *ApJ*, 535, 887
- Koranne, S. 2011, *Hierarchical Data Format 5: HDF5* (Boston, MA: Springer), 191
- Krause, M. G. H., Offner, S. S. R., Charbonnel, C., et al. 2020, *SSRv*, 216, 64
- Kroupa, P. 2002, *Sci*, 295, 82
- Krumholz, M. R. 2015, *Very Massive Stars in the Local Universe*, ed. J. S. Vink, Vol. 412 (Berlin: Springer), 43

- Krumholz, M. R., McKee, C. F., & Bland-Hawthorn, J. 2019, *ARA&A*, **57**, 227
- Kuhn, M. A., Feigelson, E. D., Getman, K. V., et al. 2014, *ApJ*, **787**, 107
- Lada, C. J., & Lada, E. A. 2003, *ARA&A*, **41**, 57
- Lancaster, L., Ostriker, E. C., Kim, J.-G., & Kim, C.-G. 2021, *ApJL*, **922**, L3
- Larson, R. B. 2003, in ASP Conf. Ser. 287 Galactic Star Formation Across the Stellar Mass Spectrum (San Francisco, CA: ASP), **65**
- Li, H., & Gnedin, O. Y. 2019, *MNRAS*, **486**, 4030
- Li, H., Vogelsberger, M., Marinacci, F., & Gnedin, O. Y. 2019, *MNRAS*, **487**, 364
- Longmore, S. N., Kruijssen, J. M. D., Bastian, N., et al. 2014, Protostars and Planets VI, ed. H. Beuther et al. (Tucson, AZ: Univ. Arizona Press), **291**
- Mac Low, M.-M., & Klessen, R. S. 2004, *RvMP*, **76**, 125
- Mandal, A., Mukherjee, D., Federrath, C., et al. 2021, *MNRAS*, **508**, 4738
- Maschberger, T., Clarke, C. J., Bonnell, I. A., & Kroupa, P. 2010, *MNRAS*, **404**, 1061
- Matzner, C. D. 2002, *ApJ*, **566**, 302
- McKee, C. F. 1999, The Origin of Stars and Planetary Systems, ed. C. Lada & N. Kylafis, Vol. 540 (Dordrecht: Kluwer), **29**
- McKee, C. F., & Ostriker, E. C. 2007, *ARA&A*, **45**, 565
- McKee, C. F., & Tan, J. C. 2003, *ApJ*, **585**, 850
- McMillan, S., Portegies Zwart, S., van Elteren, A., & Whitehead, A. 2012, in ASP, **453** (San Francisco, CA: ASP), **129**
- McMillan, S. L. W., & Hut, P. 1996, *ApJ*, **467**, 348
- McMillan, S. L. W., Vesperini, E., & Portegies Zwart, S. F. 2007, *ApJL*, **655**, L45
- Miyoshi, T., & Kusano, K. 2005, *JCoPh*, **208**, 315
- Motte, F., Bontemps, S., & Louvet, F. 2018, *ARA&A*, **56**, 41
- Oliphant, T. E. 2007, *CSE*, **9**, 10
- Ostriker, E. C., Gammie, C. F., & Stone, J. M. 1999, *ApJ*, **513**, 259
- Ostriker, E. C., McKee, C. F., & Leroy, A. K. 2010, *ApJ*, **721**, 975
- Palla, F., & Stahler, S. W. 1999, *ApJ*, **525**, 772
- Pedregosa, F., Varoquaux, G., Gramfort, A., et al. 2011, *JMLR*, **12**, 2825
- Pelupessy, F. I., van Elteren, A., de Vries, N., et al. 2013, *A&A*, **557**, A84
- Peters, T., Klessen, R. S., Mac Low, M.-M., & Banerjee, R. 2010, *ApJ*, **725**, 134
- Portegies Zwart, S., & McMillan, S. 2018, Astrophysical Recipes; The art of AMUSE (Bristol: IOP Publishing)
- Portegies Zwart, S., McMillan, S., Harfst, S., et al. 2009, *NewA*, **14**, 369
- Portegies Zwart, S. F., McMillan, S. L. W., & Gieles, M. 2010, *ARA&A*, **48**, 431
- Portegies Zwart, S. F., McMillan, S. L. W., van Elteren, A., Pelupessy, F. I., & de Vries, N. 2013, *CoPhC*, **184**, 456
- Portegies Zwart, S., Pelupessy, I., Martínez-Barbosa, C., van Elteren, A., & McMillan, S. 2020, *CNSNS*, **85**, 105240
- Portegies Zwart, S. F., & Verbunt, F. 1996, *A&A*, **309**, 179
- Rahner, D., Pellegrini, E. W., Glover, S. C. O., & Klessen, R. S. 2017, *MNRAS*, **470**, 4453
- Rahner, D., Pellegrini, E. W., Glover, S. C. O., & Klessen, R. S. 2018, *MNRAS*, **473**, L11
- Rahner, D., Pellegrini, E. W., Glover, S. C. O., & Klessen, R. S. 2019, *MNRAS*, **483**, 2547
- Rogers, H., & Pittard, J. M. 2013, *MNRAS*, **431**, 1337
- Roman-Duval, J., Jackson, J. M., Heyer, M., Rathborne, J., & Simon, R. 2010, *ApJ*, **723**, 492
- Smith, M. C., Sijacki, D., & Shen, S. 2018, *MNRAS*, **478**, 302
- Smith, R., Goodwin, S., Fellhauer, M., & Assmann, P. 2013, *MNRAS*, **428**, 1303
- Sormani, M. C., Treß, R. G., Klessen, R. S., & Glover, S. C. O. 2017, *MNRAS*, **466**, 407
- Tan, J. C., Beltrán, M. T., Caselli, P., et al. 2014, Protostars and Planets VI, ed. H. Beuther et al. (Tucson, AZ: Univ. Arizona Press), **149**
- Truelove, J. K., Klein, R. I., McKee, C. F., et al. 1997, *ApJL*, **489**, L179
- Turk, M. J., Smith, B. D., Oishi, J. S., et al. 2011, *ApJS*, **192**, 9
- Vázquez-Semadeni, E., González-Samaniego, A., & Colín, P. 2017, *MNRAS*, **467**, 1313
- Vázquez-Semadeni, E., Palau, A., Ballesteros-Paredes, J., Gomez, G. C., & Zamora-Aviles, M. 2019, *MNRAS*, **490**, 3061
- Wall, J. E., Mac Low, M.-M., McMillan, S. L. W., et al. 2020, *ApJ*, **904**, 192
- Wall, J. E., McMillan, S. L. W., Mac Low, M.-M., Klessen, R. S., & Portegies Zwart, S. 2019, *ApJ*, **887**, 62
- Weidner, C., & Kroupa, P. 2006, *MNRAS*, **365**, 1333
- Wienen, M., Wyrowski, F., Schuller, F., et al. 2012, *A&A*, **544**, A146